Laser-cleaning effects induced on different types of bronze archaeological corrosion products: chemical-physical surface characterisation

Original
Laser-cleaning effects induced on different types of bronze archaeological corrosion products: chemical-physical surface characterisation / Di Francia, E.; Lahoz, R.; Neff, D.; de Caro, T.; Angelini, E.; Grassini, S.. - In: APPLIED SURFACE SCIENCE. - ISSN 0169-4332. - STAMPA. - 573:(2022). [10.1016/j.apsusc.2021.150884]

Publisher:
Elsevier B.V.

Published
DOI:10.1016/j.apsusc.2021.150884

Laser-cleaning effects induced on different types of bronze archaeological corrosion products: chemical-physical surface characterisation

Elisabetta Di Francia [a*], Ruth Lahoz[b*], Delphine Neff[c], Tilde de Caro[d], Emma Angelini[a], Sabrina Grassini[a]

[a] Politecnico di Torino, Dipartimento di Scienza Applicata e Tecnologia, Corso Duca degli Abruzzi 24, 10129 Torino, Italy (elisabetta.difrancia@polito.it, difrancia.elisabetta@gmail.com, sabrina.grassini@polito.it, emma.angelini@polito.it)

[b] Instituto de Nanociencia y Materiales de Aragón, (CSIC Universidad de Zaragoza), María de Luna 3, 50018 Zaragoza, Spain (rlahoz@unizar.es)

[c] NIMBE/LAPA-IRAMAT, CEA/CNRS/Université Paris-Saclay, UMR3685, CEA Saclay, bat 637, 91191 Gif/Yvette, France (delphine.neff@cea.fr)

[d] CNR-Istituto per lo Studio dei Materiali Nanostrutturati, Montelibretti, Via Salaria km 29,300, Italy (tilde.decaro@cnr.it)

***Corresponding author:**

*Elisabetta Di Francia (elisabetta.difrancia@polito.it, difrancia.elisabetta@gmail.com) ORCID: 0000-0003-1874-7543

*Ruth Lahoz (rlahoz@unizar.es) ORCID: 0000-0003-4708-5577

Highlights

- Assessment of laser-cleaning induced effects on different surface structures
- Systematic study of corrosion products characterisation
- Laser-cleaning of different Cu-based archaeological artefacts
- Novelty in using a laser-scanning system to clean archaeological surfaces

Abstract

Archaeological bronzes (Cu-Sn alloys) might be different in composition and these variabilities lead to a different interaction with the environment and, if they were buried, with several chemical elements present in soils. Generally, the results is the presence of complex corrosion products layers on the Cu-based artefacts which might be protective or reactive (and so dangerous) for the artefacts preservation itself. Moreover, the corrosion products can also be unwanted because hide the drawings present/imprinted on the original metal surfaces.

So, for several reasons, it can be necessary to remove the unwanted corrosion products: laser-cleaning procedure is one of the most selective cleaning technique used.

The main goal of this work was to assess possible laser-cleaning induced surface effects on different archaeological bronzes corrosion products structures through a systematic and multi-technique compositional study.

The results of the chemical-physical characterisation performed on laser-cleaned and non-cleaned types of Cu-Sn archaeological corrosion products structures show the efficiency and the low-invasiveness of the treatment.

Keywords: laser cleaning, archaeological bronze, induced surface effect, corrosion, chemical-physical characterisation

1. Introduction

Understanding the corrosion behaviour in Cu-Sn alloys have always aroused wide interest for those that try to reproduce these "*patinas*" for both aesthetic and protective purposes [1,2]. However, the formation of corrosion layers on archaeological Cu-based artefacts is the results of complex interactions of the metal with the soil chemical-physical properties and with the environmental conditions: the corrosion mechanisms that take place lead to the complex stratified microstructures usually found [3–6]. The final surface aspect is of extremely importance for both the already mentions aesthetic and protective purposes. In this perspective, the study of corrosion phenomena and surfaces gains importance for both improving knowledge in the field of long-term corrosion and, above all, for controlling and stopping deterioration processes of ancient and historic metals in storage conditions or in museums [1,4,7–9].

1.1. Corrosion products formation on Cu-based alloys

It is known that not only the corrosive environment but also the metallurgical technique employed, the artefact chemical composition and how the corrosion attacks the object (stratification, transgranular or intergranular corrosion) play an important role in the structural transformations of Cu-based artefacts during a long-term corrosion process that leads to a steady state [3,4].

On bronzes, literature agrees on two generic models of corrosion (and corresponding deviation structures) firstly introduced and extensively studied by Robbiola and colleagues [3,4]: Type 1 and Type 2, due to cationic or anionic migrations, respectively.

Type 1 structure is characterised by the presence of two layers: a thin protective corrosion layer (*noble patina*) grown in contact with the metal overlapped by a second thicker porous layer; in that case, it is possible to find a tin-enriched corrosion layer due to a decuprification process. The inner protective red-brown layer is mainly constituted by cuprous oxides (cuprite, Cu_2O) while the generally green outer layer is constituted by different chemical compounds, in dependence of the interaction with soil constituents, oxygen and humidity. The outer layer can be characterised by low copper contents and high tin contents. Furthermore, the aging of the corrosion products leads to soil elements incorporation (O, Si, Fe, Al, Ca, P, Cl, …) and, e.g., the possible transformation of cuprous compounds in cupric compounds. As a consequence, the surface can be constituted by soil elements and copper compounds as malachite ($Cu_2(OH)_2CO_3$), brochantite ($Cu_4(OH)_6(SO)_4$), etc.

Type 2 is characterised by a three-layer structure: in presence of Cl^- ions (aggressive environment), the outer porous corrosion layer, can let penetrate the Cl^- ions through the layer creating a high concentration of chloride ions, together with tin and copper compounds, at the metal-corrosion layer interface (of the inner layer). The outer layer is characterised by copper (II) compounds, such as hydroxychlorides (atacamite ($Cu_2Cl(OH)_3$ and its polymorphs), hydroxycarbonates (malachite), hydroxysilicates and hydroxyphosphates. Between the outer and the inner layer, an intermediate layer of cuprous oxides is present. In the inner layer, this might lead to the formation of reactive cuprous chloride (nantokite, CuCl), responsible for the cyclic copper corrosion processes, well known as *bronze disease*, where the dangerous corrosion layer grows at the expense of the bulk alloy [1,3,4,6,10–12].

1.2. Laser-cleaning procedures on Cultural Heritage

As a consequence, the corrosion products (that are a multi-component material) can hide the drawings present/imprinted on the original metal surfaces or, in the worst case, they can compromise the conservation of the object itself. Therefore, the removal of the unwanted and/or dangerous corrosion products might become necessary. Since laser-cleaning (or laser-ablation, or removal) treatments are a low-invasive and highly-selective method, they have been studied for removing the unwanted and/or reactive corrosion products on several archaeological/historical materials [13–21]. On metals, the final aims are stopping possible dangerous processes and preserving the protective patina and the metal surface. Laser-ablation methods have been also preferred for the fact that they are eco-friendlier than the common chemical and mechanical methods generally used and they guarantee less risk for the operators [13,15–17,21–23].

Even so, there is a lack of sustained models explaining the laser-material interactions in the conservation field: they are usually more fundamental studies or special conservation cases more focused on the final cleaning results than on the discussion of the on going mechanisms. Only few authors reported considerations on the mechanism that occurred and on the chemical-physical characterisation of the laser effect on the surface of the artefacts [14,16,22,24–27].

This can be explained by the heterogeneity in composition of each unique cultural object: it is a complex problem to standardise cleaning procedures as a function of the interactions that occur among the laser parameters and the composition of the unwanted materials (e.g. dust or multi-material corrosion products) present on artefacts. In fact, the complex interactions, that allow laser-ablation process, are dependent from laser parameters (e.g. laser wavelength, continuous or pulsed laser, pulse duration, fluence, irradiance), optical and thermal properties of the material to remove (e.g. absorption coefficient, thermal conductivity) and surrounding environment (e.g. air, vacuum). Furthermore, the success of a laser-cleaning procedure is due to a proper combination of the laser parameters: they have to be set as a function of the properties of both the multi-component material to be removed and the underlying original surface. In that way, the interactions are confined, as much as possible, on the outmost layer occupied by the unwanted materials [28]. Recently, a more theoretical approach with experimental applications on coins has been published [29] with the final aim of assessing some laser conditions and parameters (e.g. penetration depth of the laser beam and laser fluence); however, the study was performed on modern coins.

Figure 1 proposes a model of the laser-cleaning process on Cultural Heritage Cu-based metal artefacts. The laser, thanks to complex interactions within the plasma, is able to remove (high-selective) the unwanted corrosion products (green in the picture), which absorb the laser beam, leaving the protective layer of corrosion product (brown in the picture). The metallic surface, reflecting the laser beam, is not damaged (low-invasive). So, a properly set laser is able to discriminate between unwanted and protective corrosion products, which similarly absorb the laser beam. Moreover, it makes possible to focus the ablation on specific point of persistent unwanted corrosion products.

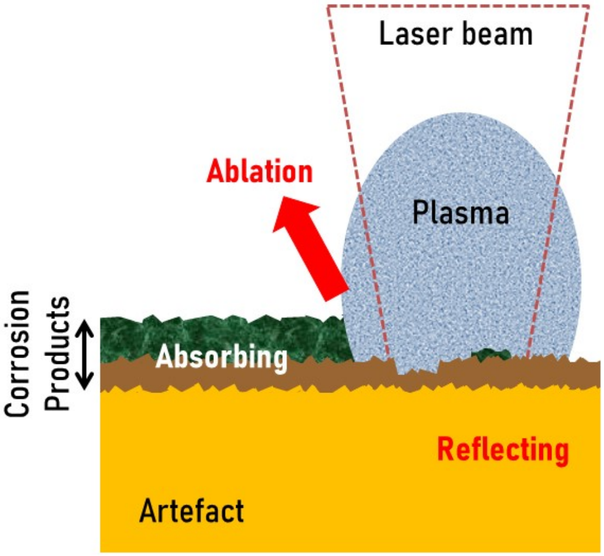

Fig. 1. Laser-cleaning ablation model for Cu-based archaeological artefacts.

This research (part of a wider project [27,30]) try to overcome to this literature lack assessing possible laser-cleaning induced surface effects (similar or different) on different types of Cu-Sn archaeological corrosion products structures through a systematic and multi-technique compositional study on laser-cleaned and non-cleaned areas.

Regardless of whether the stable corrosion products are generally preserved by conservators and restorers, and knowing the high-selectivity of the laser and that archaeological objects might present both corrosion situation on the same surfaces, this study aims to determine the effects of the laser on both stable and dangerous corrosion products.

To do this, an infrared nano-pulsed laser was used. For this kind of used wavelength, thermal laser-materials interactions (e.g. heat propagation and dissipation) are the most important laser-induced process to be considered: they allow thermal decomposition, the formation of a plasma and finally the ablation of material [28]. Moreover, the research introduces the novelty of the use of a laser-scanning system that, thanks to a dedicated software, allows to remotely move the laser on the surfaces and to control not only the laser parameters but also the geometrical parameters (scanning parameters) as the pulse overlap on X and Y axes. Video 1 shows the XY scanning movement of the laser during a treatment process over a surface.

The effect of the laser-ablation parameters applied in this article were previously studied on Cu-based reference samples presenting different artificial corrosion products, in order to assess, and not test, the procedure on archaeological objects. The previous tests, partially published in [27,31] highlighted that a shorter pulse duration is more efficient in the removal of unwanted Cu(II) corrosion layer preserving cuprous oxide layer. In addition to this, the diffuse reflectance of the corrosion crystals toward the laser wavelength, their grain size and the porosity of the layers play an important role on the laser-ablation effects.

2. Materials and methods

2.1. Laser system employed

An Yb:YAG fibre laser (Jeanologia laser, model EasyMark-20), operating in the near-IR region at a wavelength of 1064 nm was used for the cleaning treatments. The system operates in a QS regime, from 4 ns to 200 ns of pulse duration; the pulses are delivered by means of two-galvanic mirrors and are focused with a f-Theta lens with 160 mm of focal distance.

The laser system is coupled via computer with EzCAD 2.1 UNI, a vector graphic editor, with a CAD-*like* capability that enables users to perform complex surface scanning treatments in a repeatable, rapid and precise way.

Moreover, the graphic editor allows both laser parameters (e.g. output power, P, and pulse duration, t_p) and geometrical parameters, those contribute in controlling the overlapping of the pulses to be managed. Overlap on X and Y axes are adjusted for preventing undesired heat accumulation on the treated areas that might cause melting phenomena instead of ablation of the unwanted layer.

Table 1 shows the laser-ablation parameters applied. They were selected, from previous tests discussed elsewhere [27,31], as a function of the chemical composition of the corrosion products to be removed. It has to be noticed that managing the laser power, it is possible to control the pulsed power per area (fluence) and average power per area (irradiance), and so, to command the laser energy on the thickness of the unwanted corrosion product layers. In addition to this, 30 µm of spot diameter and 300 mm/s of scan speed were used for the overlapping on X-axis while 15 µm of interlining was used for the overlapping on Y-axis: in that way, a proper overlap was guarantee.

Tab. 1. Laser cleaning performed on the archaeological samples.

	Laser parameters				**Geometrical parameters**	
Test	*Power,* *P (W)*	*Fluence,* *F* (J/cm^2)	*Irradiance,* *I* (W/cm^2)	*Pulse Duration,* t_p *(ns)*	*Scanning speed,* v_{scan} *(mm/s)*	*Interlining,* d_L *(mm)*
1	0.23	1.63	406.73	4	300	0.015
2	0.73	5.16	1290.94	4	300	0.015

2.2. Archaeological samples

Two archaeological coins coming from a private collection were the objects of this study. No information about the provenance contexts and recent history of the artefacts are available. Despite this, both coins present an ancient-looking Cu-based alloy appearance.

Coin 1 is a *Dupondio Marco Aurelio*, a Roman Empire bronze coin (2nd century A.D. dated). On the *recto* side (observe face), it is visible the head of the emperor while on the *verso* side (reverse face) it is observable a figure (Fig. 2, above). The coin is 8.8081 g-in mass and 22 × 23 × 3 mm^3-in size. The archaeological corrosion products are well adherent to the substrate, compact and present a shining yellow-green/dark green colour on both sides. The coin seems to be in a good conservation state. The analyses were performed on the obverse side, less rough due to the drawn.

Coin 2 is a *Follis Massenzio*, a Roman Empire bronze coin (4th century A.D. dated). On the *recto* side (observe face) it is visible the head of the emperor while on the *verso* side (reverse face) it is observable a temple (Fig. 2, below). The coin is 5.8555 g-in mass and 24 × 25 × 2 mm^3-in size. The analyses were performed on the reverse side: even if the corrosion products are well adherent to the substrate on both sides, they present a more uniform greenish corrosion layer on the reverse side than on the observe side. The corrosion products were not grew in a uniform way on the surfaces. The coin seems probably affected by the *bronze disease*.

Fig. 2. High-resolution coin photograph. Above: Dupondio Marco Aurelio*,* recto *and* verso *sides; below:* Follis Massenzio*,* recto *and* verso *sides.*

2.3. Sample preparations and characterisations

Morphological, microstructural and chemical-physical techniques were used for characterising the laser-cleaned and non-cleaned areas in order to observe any modification due to the laser-treatment process on surfaces and on sections.

2.3.1. Cross-section preparations

The coin was previously cut in fragments with a diamond blade; afterwards, the samples were rinsed in ethanol in ultrasonic bath for 5 min, dried and then submitted to laser ablation in order to have a defined area to treat. After that, the cross-sections were prepared by embedding the specimen in epoxy SpeciFix-20-Struers resin and cutting them with a diamond blade, in parallel to the laser scanning direction. After that, they were polished with 500-grid to 4000-grid SiC papers and then with 6 µm to 1 µm-grid cloths: ethanol was used instead of water in order to prevent any solubilisation of the corroded compounds and diamond pastes were used with the cloths. Then, the cross-sections were rinsed in isopropyl alcohol in ultrasonic bath for 10 min and well dried.

For the bulk analyses, an etching aqueous ferric chloride solution (5 g $FeCl_3$, 15 ml HCl (40 % conc.), 60 ml H_2O) suitable for archaeometallurgical Cu-based alloys was used to produce grain contrast [32–34]. The procedure was carried out at room temperature.

2.3.2. Characterisations

High-resolution digital photographs (4000 × 3000 pixel^2) were acquired using a digital camera Panasonic Lumix G2 equipped by a stand with a 3000 K lamp.

Optical microscopical (OM) images were acquired by means of a Leica DMI5000M microscope and an Olympus BX51 microscope equipped with a Nikon EOS camera operating in bright and in dark-field modality. Respect to the bright-field (BF) observations, the dark-ones (DF) are able to discriminate the complex nature of archaeological stratified copper-alloys corrosion products [5,6,35–37]. In fact, DF-OM red-brown colour is associated to the presence of Cu(I) compounds as cuprous oxide (cuprite), the green colour to the presence of Cu(II) compounds as hydroxycholoride polymorphs (e.g. atacamite, clinoatacamite, botallackite) or carbonates (e.g. malachite) while the yellow-orange colour to cuprous chloride (e.g. CuCl) [5,6] or a mix of copper and nanometric tin oxides [36].

These instruments are henceforth named in the text as *OM-Leica* and *BF/DF OM-Olympus*, respectively.

EDS data and μRaman spectra were used to assess the composition of the different-in colour corrosion products.

Electron microscopical data were acquired by means of three scanning electron microscopes (SEM):

- Field Emission Scanning Electron Microscopy (FESEM, Supra 40 model, Carl Zeiss) operating in secondary electron and in in-feld emission modes and coupled with an Energy Dispersive Spectroscopy (EDS INCA x-sight, Oxford instruments);
- Scanning Electron Microscopy (SEM, FEI Quanta Inspect 200 model) coupled with an Energy Dispersive Spectroscopy (EDS EDAX Genesis);
- High vacuum Field Emission Scanning Electron Microscope (FESEM, Merlin model, Carl Zeiss) coupled with an Energy Dispersive Spectroscopy (EDS INCA x-sight, Oxford instruments).

These instruments are henceforth named in the text as *FESEM-Supra*, *SEM-FEI* and *FESEM-Merlin*, respectively.

μRaman analyses were carried out at room temperature by means of:

- Renishaw Invia device equipped with a doubled Nd:YAG laser (532 nm), under a Leica x50/0.85 microscope objective. The laser power on the sample surface was set at ≈ 500 μW in order to avoid the thermal transformation of the analysed phases.
- Renishaw RM2000 instrument with a Leica optical microscope. Measurements were performed using the 50x and the 100x objectives and a 785 nm excitation line of an Ar^+ laser. With the 100x objective and the 50% filter, the real output power laser is about 1.58 mW.

Both instruments are equipped with a Peltier cooled charge-coupled device (CCD) camera in conjunction with the optical microscope and, for both, the laser spot diameter was of about 1 μm.

The data were acquired with Wire3.3 Renishaw software and the experimental spectra were compared with the spectra collected in a database composed from synthetic or commercial powders obtained in laboratory and with references reported in RRUFF Project database [38] and in literature [10,36,39–42].

These instruments are henceforth named in the text as *µRaman-green laser* and *µRaman-red laser*, respectively. The µRaman-green laser instrument was used on Coin 2 while the µRaman-red laser device was used on Coin 1.

XRD spectra were collected by a Philips X'PERT PW3040/00 diffractometer and a Panalytical X'PERT PRO diffractometer, both presenting a Cu target. Patterns were acquired using a 10 mask, ¼ and ½ slites from 8° to 70° 2 θ and a step size of 0.02° per 2 s and from 8° to 70° 2 θ and a step size of 0.013° per 30.6 s, respectively.

Qualitative identifications of the reflection patterns were done with the X'Pert HighScore Plus v3.0e software by comparison with ICSD database.

3. Results and discussion

3.1. Metallographic and corrosion products structures observations

Table 2 shows the figures of the chemical compositions determined on the bulk of the two coins. Both artefacts are low-tin content bronze coins with variable presence of lead; the presence of silver was detected only on Coin 2.

Tab. 1. EDS bulk determination for Coin 1 and Coin 2.

wt. %	Cu	Pb	Sn	Ag	Zn	Fe	Ni
Coin 1	90.20	4.72	4.10	/	0.64	0.17	0.17
Coin 2	81.95	11.00	4.10	2.95	/	/	/

Figure 3 (A and B) displays the Coin 1 bulk (OM-Leica and SEM-FEI): a complex microstructure characterised by the presence of almost equi-axed and quite variable-in size polygonal grains without the presence of a preferential orientation. Twin lines, straight lines and globular elements along the main grains are also visible. The Figure illustrates also the SEM-FEI-EDS analyses of the alloy phases (B and C): Sn and Cu were observed in the big grains with and without strain lines (point 2 and 3 in the picture). The presence of Pb was identified in the globular shapes: in conjunction with Sn (in the darkest areas, point 5 in the figure) and without impurities (in the brightest areas, point 4 in the picture). The presence of almost spherical intergranular grains composed of Cu, Sn, Pb and with impurities of S was also detected (point 1 in the picture).

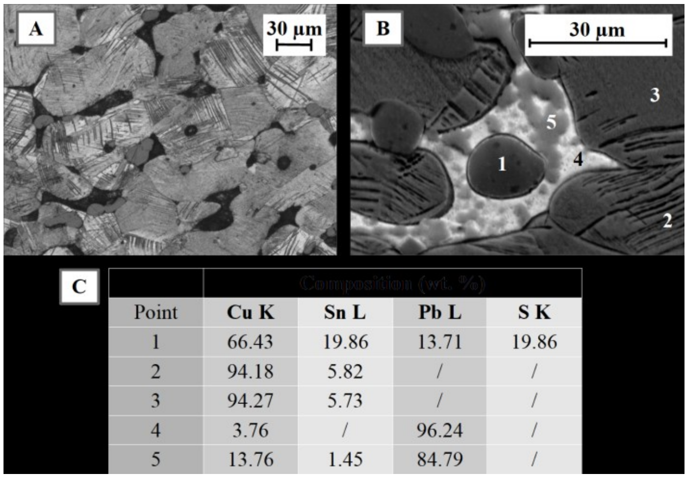

	Composition (wt. %)			
Point	**Cu K**	**Sn L**	**Pb L**	**S K**
1	66.43	19.86	13.71	19.86
2	94.18	5.82	/	/
3	94.27	5.73	/	/
4	3.76	/	96.24	/
5	13.76	1.45	84.79	/

Fig. 3. Coin 1: microstructure of coin's bulk after etching in aqueous $FeCl_3$ *solution. OM-Leica image (A); SEM-FEI backscattered electron image (B); indication of the EDS punctual analyses with corresponded EDS composition (C).*

Figure 4 (A and B) shows the Coin 2 bulk (OM-Leica and FESEM-Supra): this coin presents a fine grain structure characterised by the presence of quite polygonal grains and a probable oriented segregation, flattened out along the coin length; several twins and straight lines are visible.

The Figure illustrate also the FESEM-Supra-EDS analyses of the alloy phases (B and C). The big grains with and without strain lines are mainly composed of Cu with the presence of Sn (point 2 and 5 in the picture). The segregation, flattened out along the coin length, are mainly composed of Pb and Cu with the presence Sn or some impurities of Ag (point 1 and 4 in the picture). The very bright irregular shapes of the picture (point 3), localised at the interior of the Pb segregations, are characterised by the strong presence of Ag in conjunction with Pb and Cu: EDS maps of Pb and Ag show their positions. Since the silver is associated to the lead, probably the silver was part of the ore of lead (*argentiferous galenas*).

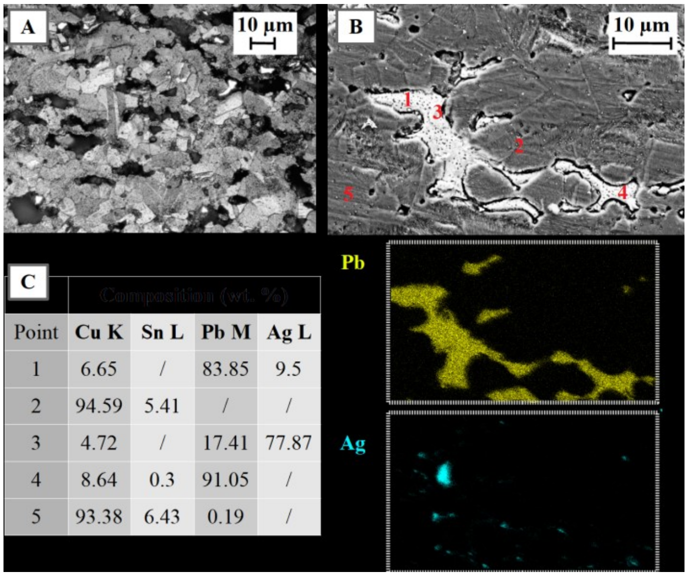

	Composition (wt. %)			
Point	Cu K	Sn L	Pb M	Ag L
1	6.65	/	83.85	9.5
2	94.59	5.41	/	/
3	4.72	/	17.41	77.87
4	8.64	0.3	91.05	/
5	93.38	6.43	0.19	/

Fig. 4. Coin 2: microstructure of coin's bulk after etching in aqueous $FeCl_3$ *solution. OM-Leica image (A); FESEM-Supra-secondary electron image and correspondent maps of the Pb and Ag elements (B); indication of the EDS punctual analyses with corresponded EDS composition (C).*

Concerning the corrosion products, OM observations, performed on the cross-sections of the non-cleaned areas, revealed a different situation for the two coins. Figure 5 compares the high-resolution images of the coins in association with their typical internal structure found.

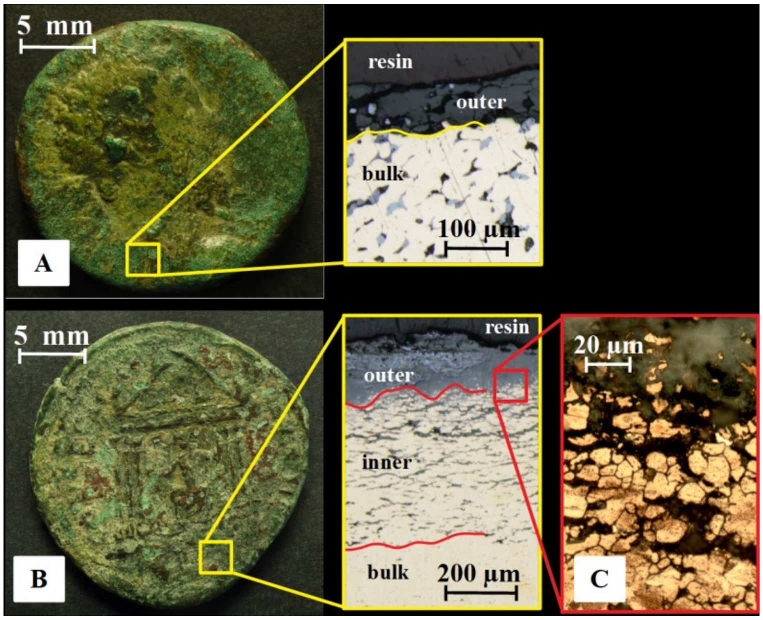

Fig. 5. High-resolution coin photograph and OM cross-section images of the corrosion product structures: (A) Coin 1 and related bright-filed OM-Olympus observation; (B) Coin 2 and related bright-filed OM-Olympus observation; (C) particular of Coin 2: OM-Leica metallographic image on the etched cross-section.

On Coin 1 (A), the corrosion products formed a regular outer compact layer, up to 105 µm-in thickness over the original surface while on Coin 2 (B), it was possible to highlight the presence of an outer compact corrosion products layer, up to 200 µm-in thickness, and a partially corroded inner layer, up to 800 µm-in thickness. This intergranular corrosion behaviour towards the bulk of Coin 2 was also supported by metallographic data, visible in the figure (C).

From these data, it is possible to conclude that the two bronze coins both present a typical structure of recrystallised grains with the presence of mechanical deformation probably due to mechanical working during the minting process [32]. They have a different alloy composition and underwent to a different corrosion process.

3.2. Corrosion products layer thickness: laser-cleaning reductions

Figure 6 shows, for each coins, cross-sections comparison in DF-OM-Olympus of the non-cleaned and laser-cleaned areas (Test 1 and Test 2). As it is possible to see in the Tables, Test 2 affected more the outer corrosion products layers, detectable in an average thickness reduction up to ≈ 44 µm for Coin 1 and ≈ 41 µm for Coin 2 while for Test 1, the average thickness reduction was up to ≈ 23 µm for Coin 1 and ≈ 15 µm for Coin 2.

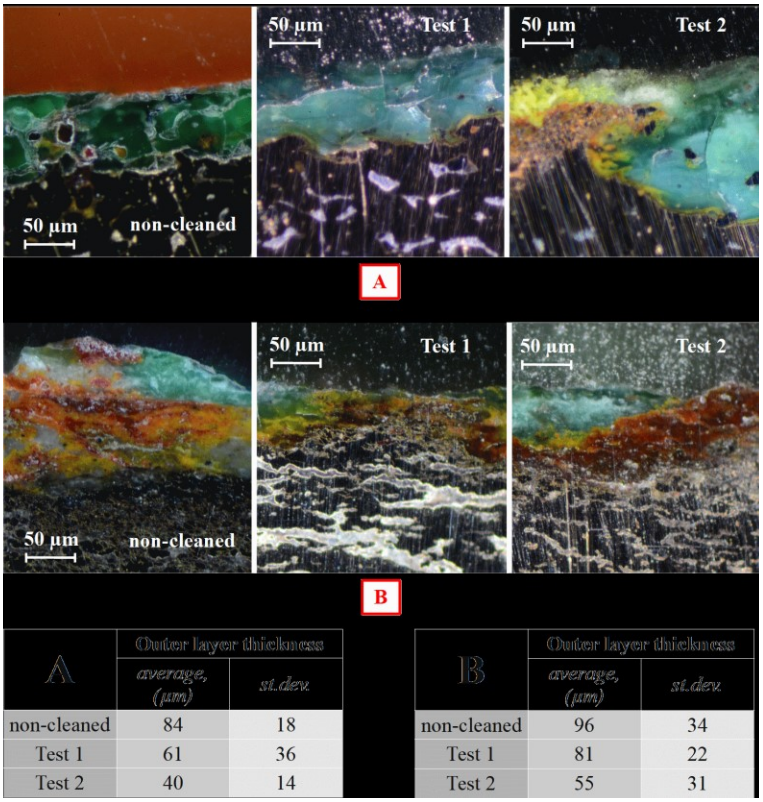

A	Outer layer thickness	
	average, (µm)	st.dev.
non-cleaned	84	18
Test 1	61	36
Test 2	40	14

B	Outer layer thickness	
	average, (µm)	st.dev.
non-cleaned	96	34
Test 1	81	22
Test 2	55	31

Fig. 6. DF-OM-Olympus cross-section images of the typical corrosion product structures: (A) Coin 1; (B) Coin 2 and corresponding tables layer thickness.

Despite the thickness reduction, the picture highlights that the structure of the corrosion products is not substantially changed. On Coin 1, the laser interacted only with the surface of the outer compact corrosion products layer, probably affecting less the corrosion products present in the cradles-cavities. This is evident on the typical structure observed on Test 2 area: a thinner DF yellowish/greenish layer, instead of a uniform DF green layer, is overlapped to a DF orange layer interconnected with the metal alloy. The cradles-cavities, when present, are still green/turquoise green in DF with a thinner yellowish/reddish layer in contact with the metal.

On Coin 2, a more stratified and complex structure is present: a DF turquoise green colouration above a thinner DF red-brown-in colour layer and spot-areas where only red-brown colouration. Yellowish-in colour areas or very thin layers are presented between the green and the red-brown layers. Despite this, a similar laser effect is detectable respect to Coin 1: a reduction of the DF green layer is present also in the cradle-cavities treated with Test 2; on this coin, a yellowish/reddish thick layer is always present.

3.3. Coin 1 archaeological corrosion products characterisation: laser-cleaning effects

XRD analyses on the non-cleaned surfaces of Coin 1 (Fig. 7) identified the presence of the main elements alloy (Cu, ICSD code: 98-005-3757; $Cu_{3.84}$-$Sn_{0.12}$, ICSD code: 98-062-9282) and several corrosion products as cuprite, cassiterite and lead oxide (Cu_2O, ICSD code: 98-006-3281; SnO_2, ICSD code: 98-009-0609; PbO_2, ICSD code: 98-007-7648).

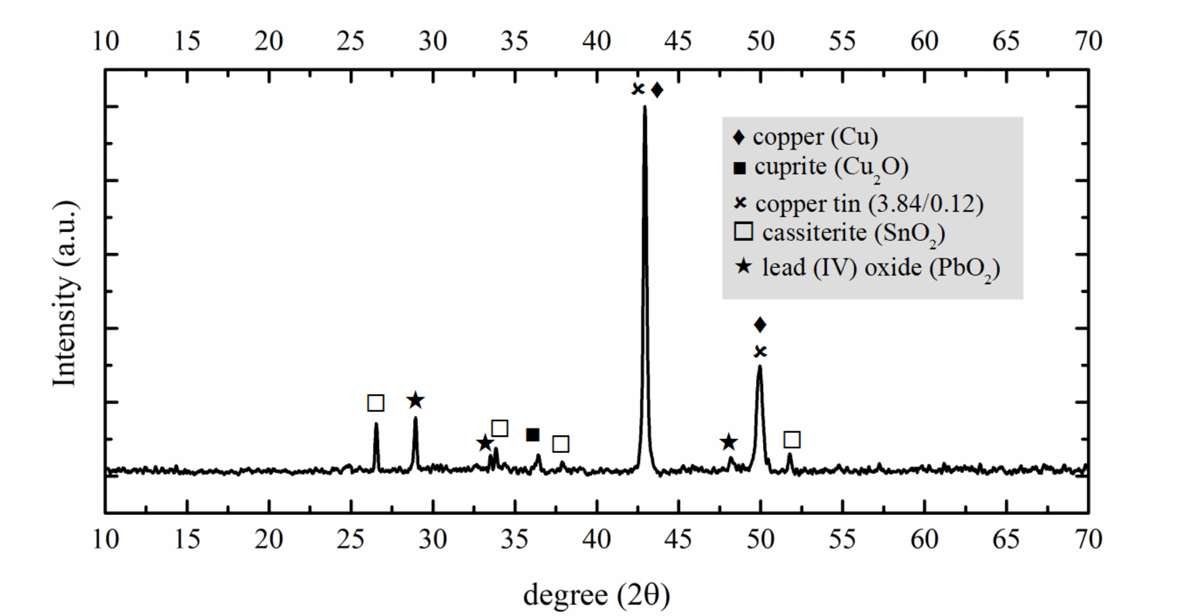

Fig. 7. XRD patterns collected on surfaces non-treated areas of Coin 1.

Concerning the chemical-physical characterisations, µRaman-red laser and FESEM-Supra-EDS analyses were performed on both the non-cleaned and the laser-cleaned Test 2 cross-sections, the test that affected more the corrosion products.

Figure 8 summarises and compares the typical compositional data acquired on Coin 1: BF and DF-OM-Olympus images and corresponding μRaman-red laser and FESEM-Supra-EDS analyses.

As shown in the image, the outer compact layer of corrosion products (dark grey in BF) appeared quite uniform with agglomeration of one or more mineralogical phases with inside speared globular spots (light grey in BF). In DF modalities, the compact layer appears green (associable to Cu(II) compounds, A in the pictures) while the most part of the globular spots appear black (points D and E in the pictures). Few globular spots acquired a red/brown colouration (associable to Cu(I) compounds, point D in the pictures) while some crystals (point B in the pictures) and some areas especially in contact with the metal (C in the pictures) appear yellow/orange in DF.

μRaman and EDS analyses confirmed those compositional hypotheses identifying the probable presence of azurite ($Cu_3(CO_3)_2(OH)_2$) and the possible presence of malachite ($Cu_2(CO_3)(OH)_2$) in the upper part of the outer layer (spectrum *A*, pie chart *A*) and the presence of cuprite (Cu_2O) [6,40,43] in the areas more in contact with the metal (spectrum and pie chart *C*). The azurite compounds was identified considering a shift of the spectra respect to the data reported in literature [41,44,45]. This shift can be explained with geometrical matters: the fluorescence component was delayed and this can create a shift; moreover a mix of azurite and possible malachite can explain this shift and also their possible presence in a nano/micro-crystalline form. In addition to this, by the fact that these identifications are performed on ancient compounds, azurite and malachite are very close in structure, azurite is lower stable than malachite and it can be converted in malachite [46], the presence of this other carbonates has not to be excluded.

Regarding the globular spots, not all of them were possible to be analysed by μRaman due to microscope resolution. Only in some spots/crystals, the presence of a mix of cuprite (Cu_2O) [6,40,43] and cerussite ($PbCO_3$) [41] was identified in the yellow/orange *B* globular spot/crystal (spectrum and pie chart *B*). Throughout FESEM images and EDS analyses it was possible to detects globular spots of a mix of copper and other soil elements (S and Fe in that case) compounds (*D* pie chart) and globular spots of cerussite, due to the high amount of lead (*E* pie chart).

Additionally, EDS analyses highlighted, respect to the bulk composition, a common higher amount of Pb (≈ from 4 wt.% to 7wt.%) and especially of Sn (≈ from 5 wt.% to 17 wt.%). Moreover, the higher presence of tin suggested the identification of the yellow/orange DF colouration as the presence of a mix of copper and nanometric tin oxides instead of cuprous chlorides [10,36]. In addition to this, the presence of a Raman band around 625 cm^{-1} and the XRD detection of cassiterite (SnO_2) reinforced the interpretation of the presence of Sn(IV) in a nanometric size mixed with cuprous oxide.

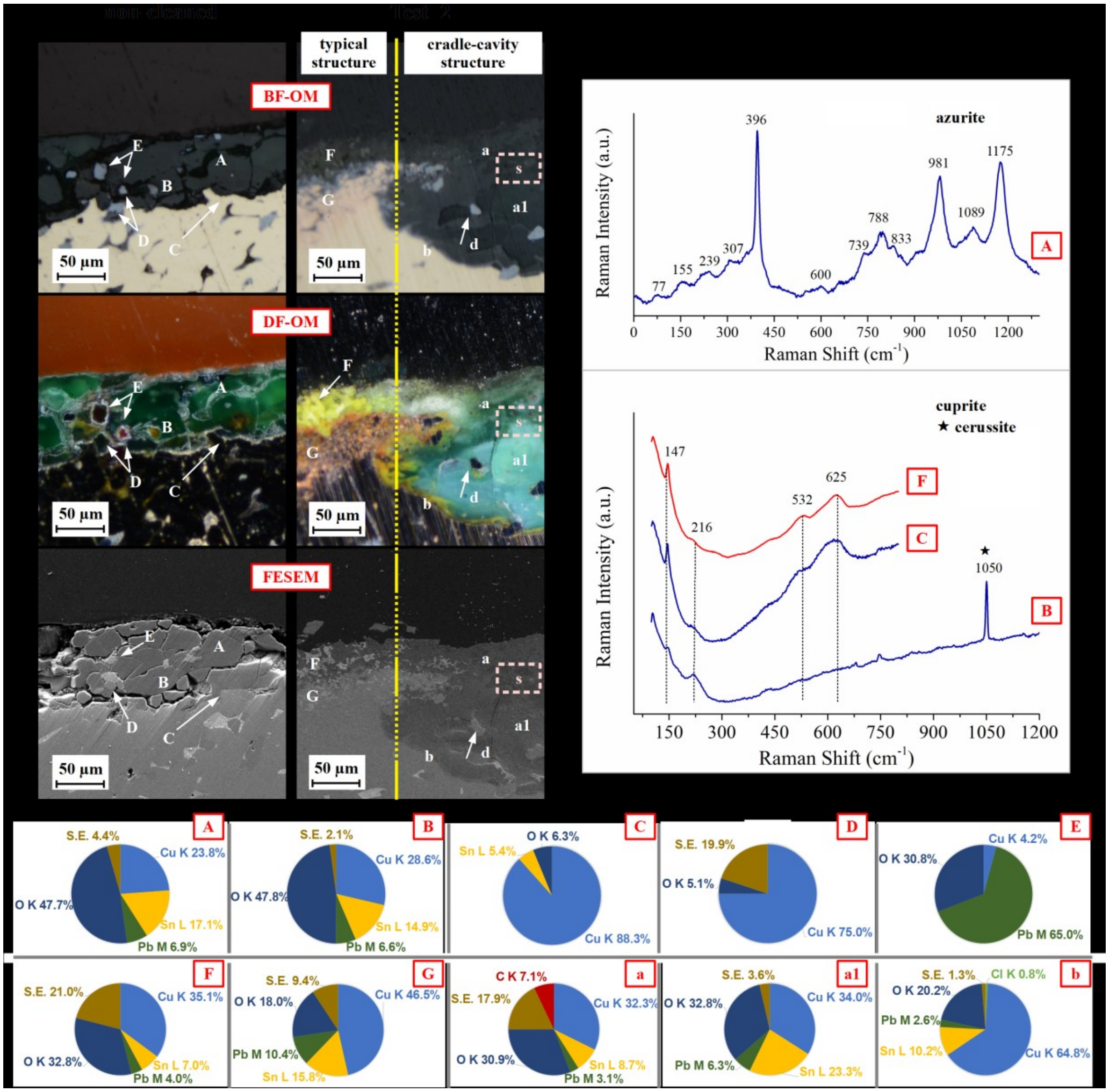

Fig. 8. Coin 1: chemical-physical characterisations comparison. BF-OM-Olympus, DF-OM-Olympus and FESEM-Supra-secondary electron images and µRaman-red laser and FESEM-Supra-EDS data acquired on non-cleaned and laser-cleaned Test 2 cross-sections (blue line: non-cleaned cross-sections; red line: laser-cleaned cross-section; pink dashed line: it highlights a specific area; S.E., Soil Elements; amounts expressed in wt.%).

On the laser-cleaned sample, a different behaviour of the laser-materials interactions was detected between the typical corrosion structure and the few cradle-cavities present. Under ablation conditions, the typical corrosion structure (*A* in the picture) disappeared leaving the place to a thinner DF yellowish/greenish layer (F area, spectrum and pie chart). This layer is characterised by the presence of cuprite associated to an increase of Cu (≈ from 23 wt.% in *A* to up to 35 wt.% in *F*) and a reduction of Pb (≈ from 7 wt.% in A to 4 wt. %) and Sn (≈ from 17 wt.% in *A* to 7 wt.%) respect to the non-cleaned green layer. Under this layer is always present a DF orange layer (*G* area and pie chart) interconnected with the metal alloy and characterised by the presence of O, Cu, Sn and Pb in different percentage. Particulars of the *F* and *G* layer are illustrated in Figure 9: the layer *G* is more structured in crystals with always a significant presence of Sn (≈ 30 wt.%) and variable presence of Pb (≈ 36 wt.%, point 4 in the picture) or Zn (≈ 32 wt.%, point 3 in the picture) in association to other soil elements as iron and/or silicon. On the contrary, the layer *F* is less structured and present higher amounts of O and Cu (points 1 and 2 in the picture).

Regarding the few cradle-cavities (Fig. 8), the corrosion structure appeared less affected by the laser: in BF they were completely dark grey with speared light-grey globular spots and a thin light-grey layer at the bottom of the cradle-cavity, in contact with the metal. In DF, the dark-grey area acquired a green (*a* area and pie chart) and a turquoise-green (*a1* area and pie chart) colour, characterised by a similar amount in O and Cu but a higher amount of soil element in the upper green area and a higher amount of Sn and Pb in the inner turquoise-green area. At the interfaces between these two areas, another structure was highlighted (*s* area): a detail is shown in Figure 9; silver is the main element of this inlet structure (5 point and pie chart).

Moreover, the thin DF yellowish/reddish layer at the bottom of the cradle-cavity is mainly composed of Cu, O, Sn and Pb (*b* area and pie chart) denoting a considerable reduction of soil elements and the presence of Cu(I) compounds. Finally, the DF black globular spots (*d* area) are characterised by the presence of a matrix with a high amount of Cu and S and by the presence of small dots of Cu, S and Zn, as it is visible in the details of Figure 9-d (respectively 6 and 7 pie charts).

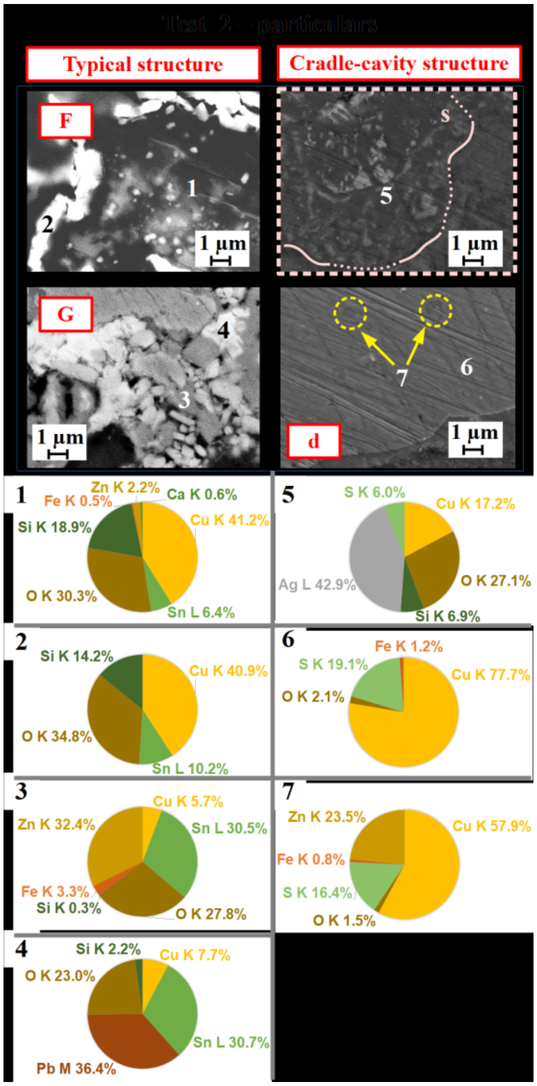

Fig. 9. Coin 1: particulars (from Fig. 8) of the effect of the laser ablation Test 2 condition on the typical corrosion structure and on a cradle-cavity structure. FESEM-Supra images and respective EDS data (pink dashed line: it highlights the specific area of Fig.8; S.E., Soil Elements; amounts expressed in wt.%).

In light of these findings, Coin 1 presented a thick outer corrosion product layer composed of copper (II) compounds as azurite/malachite and other soil elements and an inner layer were cuprous oxides were mixed with lead (cerussite) and tin (cassiterite) and the presence of soil elements is less significant. Moreover, a general high enrichment in tin and low enrichment in lead was highlighted in the outer layer. This is explained as a decuprification process with an enrichment of tin in the layer. However, the µRaman identification of tin compounds is difficult probably due to their amorphous structures and/or their presence in a nanometric size [6,10,36]. In addition to this, the azurite/malachite presence, in the upper part of the outer layer, is explained as a migration of Cu ions through the porous tin oxides layer that leads to the formation of Cu(II) compounds in contact with oxygen and soil [4,6]. Thus the presence of azurite/malachite confirms the provenance of the coin from an extensive burial in soil period: the azurite is a rare corrosion products mainly found on object buried in soils in presence of elevated hydrogen carbonate activity [6,46]. Regarding the globules of the compact corrosion layer those present different DF colours and EDS compositions, they can be identified as originally lead globules (see SEM-EDS bulk characterisation) that corroded, forming as in that case, cerussite, and subsequently were replaced by cuprite [47].

On this basis, it is possible to confirm that Coin 1 is an original Cu-Sn coin buried in soil for a long time and presents a Type-1 corrosion structure, as defined by Robbiola and colleagues [3,4].

On this corrosion situation, the laser ablation carried out at an irradiance of 1290.94 W/cm^2 was able to reduce, in a more efficient way, the thickness of the upper corroded layer decreasing the amount of tin, lead and oxides compounds and increasing the amount of copper and soil elements in different percentage. The laser cleaning evidenced also the presence of an inner layer characterised by tin and lead enrichments: this can be explained with the presence of an external porous layer characterised by agglomeration of one or more mineralogical phases (nano/micro-crystalline) partially transparent to the laser wavelength that led the laser penetrate to the inner layer. The high increase of the zinc element in this area can come from the black globules those interacted with the laser and after the treatment disappeared. Instead, when the laser ablated a cradle-cavity, it reduced the upper part of the corroded layer, detectable from a reduction of tin, lead and oxides compounds in conjunction with an increase of copper and soil elements, but, due to the depth of the cradle, it did not reach the bottom.

3.4. *Coin 2 archaeological corrosion products characterisation: laser-cleaning effects*

On Coin 2, XRD analyses (Fig. 10) on the non-treated surfaces identified the presence of copper, the main alloy (Cu, ICSD code: 98-005-3757) and the presence of several corrosion products (cuprite, Cu_2O, ICSD code: 98-003-8233; cassiterite, SnO_2, ICSD code: 98-003-9177; minio, Pb_3O_4, ICSD code: 98-002-9094). Some of the XRD patterns found can be associated to probable interactions with the soil elements (cotunnite, $PbCl_2$, ICSD code: 98-020-2130; chlorine, Cl_2, ICSD code: 98-001-8154; cerussite, $PbCO_3$, ICSD code: 98-024-7490).

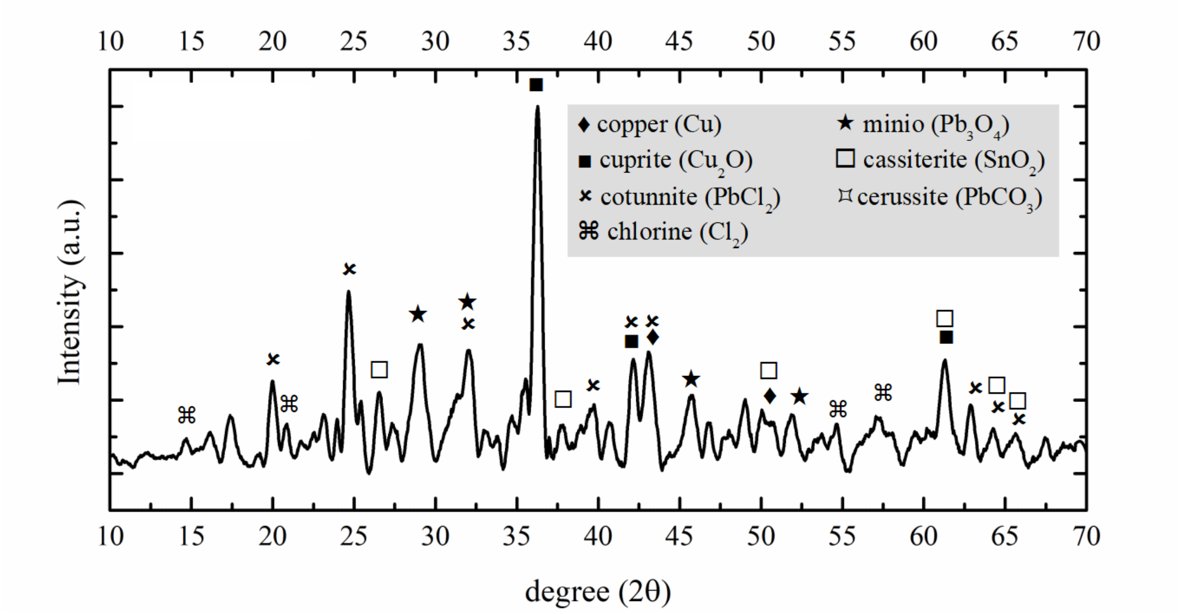

Fig. 10. XRD patterns collected on surfaces non-treated areas of Coin 2.

Figure 11 summarises and compares the typical compositional data acquired on Coin 2, on both non-cleaned and laser-cleaned Test 2 cross-sections: DF-OM-Olympus images and corresponding μRaman-green laser and FESEM-Supra-EDS analyses. The Test 2 images show the cases of both a typical corrosion structure and a sporadic presence of a cradle-cavity.

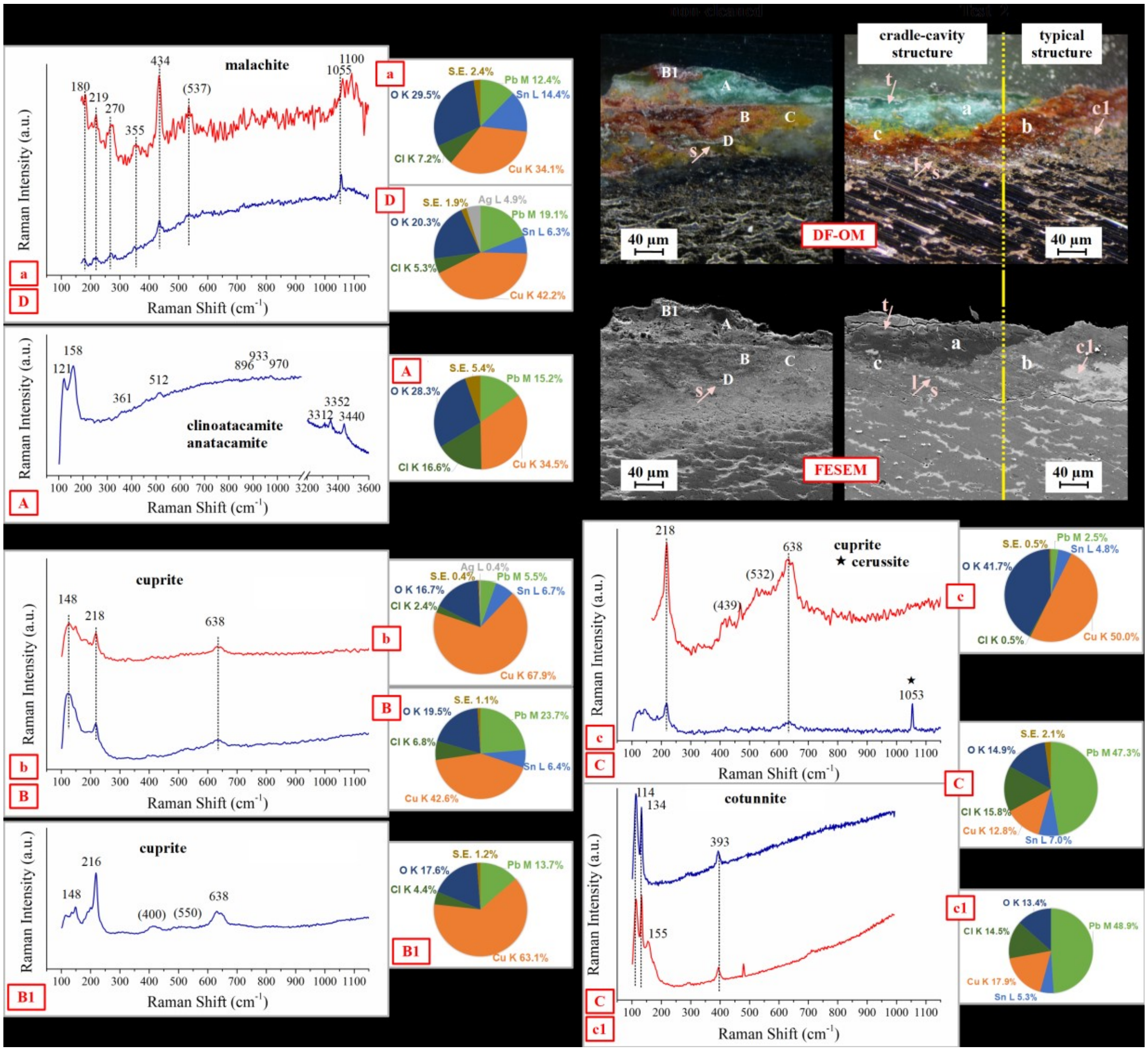

Fig. 11. Coin 2: chemical-physical characterisations comparison. DF-OM-Olympus and FESEM-Supra-secondary electron images and µRaman-green laser and FESEM-Supra-EDS punctual data acquired at the same location on non-cleaned and laser-cleaned Test 2 cross-sections (blue line and capital letter: non-cleaned cross-sections; red line and lower letter: laser-cleaned cross-section; pink arrows and letters highlight specific particulars points; S.E., Soil Elements; amounts expressed in wt.%).

The turquoise-green and the green DF areas were associated to the presence of both hydroxycholoride polymorphs and carbonates compounds. µRaman peaks (points *a* and *D*, in the pictures) highlighted the presence of malachite [6,40] while the peaks (point *A*, in the pictures) were identified as a polymorph of atacamite, probably clinoatacamite as reported in [39,41,42] and/or anatacamite (peaks at 970, 933, 896, 512, 361, 158 and 121 cm^{-1}) as reported in [42]. EDS analyses (pie charts *A*, *a* and *D*) detected a general high content of O in the range of about 20 wt. % to 30 wt. %; in the point of the hydroxycholoride polymorphs identification (*A*), a higher presence of Cl (≈ 17 wt. %) was confirmed respect to points *D* and *a*.

The DF brown-in colour areas (points *B* and *b*, in the pictures) resulted mainly composed of cuprite [6,40,43] associated with a consistent reduction of Cl (≈ from 7 wt.% to 2wt.%) and an increase of Cu (≈ from 43 wt.% to 68wt.%) between the non-cleaned and the laser-cleaned areas, as shown by the EDS pie charts (*B* and *b*). The DF red area (point *B1* in the pictures), always identified as cuprite [6,40,43], presented an EDS composition characterised by the absence of Ag and Sn (*B1* pie chart).

The DF yellow-orange-in colour areas (points *C* and *c*, in the pictures), are composed of several lead, copper and tin compounds. µRaman peaks identified the presence of cuprite and the EDS analyses (pie charts *C* and *c*) suggested the presence of copper and tix oxides: DF-OM observations, µRaman and EDS analyses, in accordance to [10,36], suggested the presence of a mix of copper and nanometric tin oxides. XRD detection of cassiterite (SnO_2) reinforced this interpretation. Moreover, on the non-cleaned areas (*C*), the µRaman peak at 1053 cm^{-1} and the high EDS content percentage of O and Pb (respectively, ≈ 15 wt. % and ≈ 47 wt. %, pie chart *C*) evidenced the presence of cerussite ($PbCO_3$) [41] mixed with the other components of the yellow-orange area. A so higher amount of of Pb (≈ 47 wt. %) and Cl (≈ 16 wt. %) respect to the EDS amounts on the brown areas (respectively, ≈ 24 wt. % and ≈ 7 wt. %, *B* pie chart) can be explained by another µRaman spectrum acquired in the same yellow-orange area (*C*), that highlighted the possible presence of cotunnite ($PbCl_2$) [41,48] and/or nantokite (CuCl; identified from laboratory database). A similar spectrum was acquired on the laser-cleaned area *c1* too; also in that case, the EDS analysis (*c1* pie chart) differs, from the non-cleaned area, only for the absence of the soil elements. For both spectra, their shape and peak positions (114, 134, (155) and 393 cm^{-1}) seem to be close to nantokite and/or cotunnite compounds. So, it is possible to hypothesis the presence of metallic salts, difficult to identify further: these salts are generally not very well crystallised and so they are difficult to be detected by XRD. Although this, the presence of the cotunnite (possibly in a nano/micro-crystalline form) could be attested, for the EDS data acquired in the same area (the percentage ratio in weight of Pb and Cl) and the XRD pattern. Moreover, with the EDS composition found in these areas (*C* and *c1*), it is possible to guess the presence of a compound with Cu, Pb, Sn and Cl. Therefore, important amounts of lead, copper and chlorine were presented in an area at the interfaces between the *B* and *b* corrosion areas and the inner corrosion layer (respectively, up to ≈ 49 wt. %, up to ≈ 18 wt. % and up to ≈ 15 wt. %, point *c1*). Moreover, the presence of a crack is visible at the interfaces between the inner corrosion layer and the upper layers.

EDS analyses always detected the presence of Cl and Pb, even if in several points of analysis with a variable amount, while the presence of Sn and, even more, the presence of Ag were concentrated in the point of analysis in the lower part of the outer corrosion products layer/intermediate layer. This is more visible on the compositional maps, acquired by FESEM-Merlin-EDS, of both non-cleaned and laser-cleaned cross-sections, shown in Figure 12. The maps suggested the presence of a demarcation line enriched in silver, chlorine, tin and lead at the intermediate corrosion products layer, near the interface with the inner corrosion products layers. The inner corroded layer is mainly composed of lead and chlorine strictly interconnected with the metal matrix of copper.

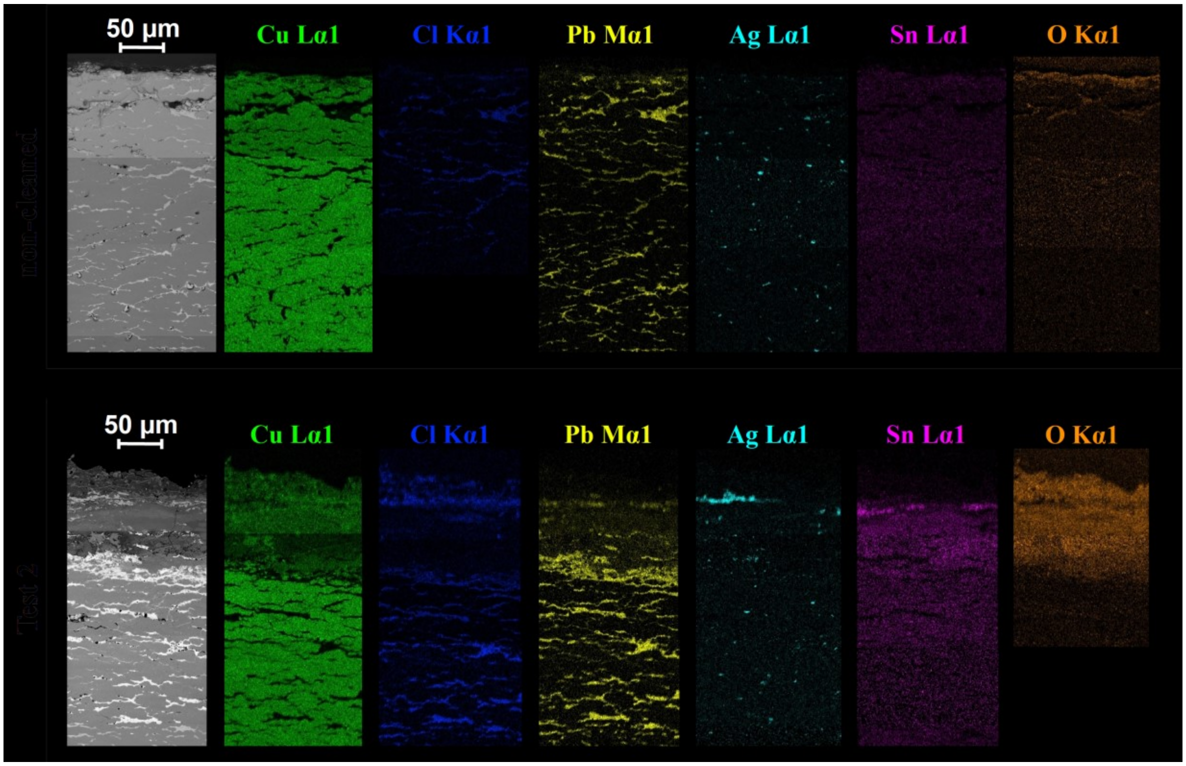

Fig. 12. FESEM-Merlin-EDS maps of non-cleaned and laser-cleaned Test 2 cross-sections of Coin 2.

Particulars of the outer corrosion products layer cross-sections of Coin 2, in the area of the demarcation line are illustrated in Figure 13-A (*D* area- non-cleaned sample) and Figure 13-B (*a*/*c* areas - laser-cleaned samples). In those areas, EDS analyses identified a higher segregation/migration of silver (up to 62 wt. %, points *s* in the pictures) on both samples and areas of lead agglomeration (up to ≈ 68 wt. %, point *l* in the picture). Moreover, a high dispersion of tin (up to ≈ 27 wt. %, point *t* in the picture) was found in the *a* area (Figure 13-C).

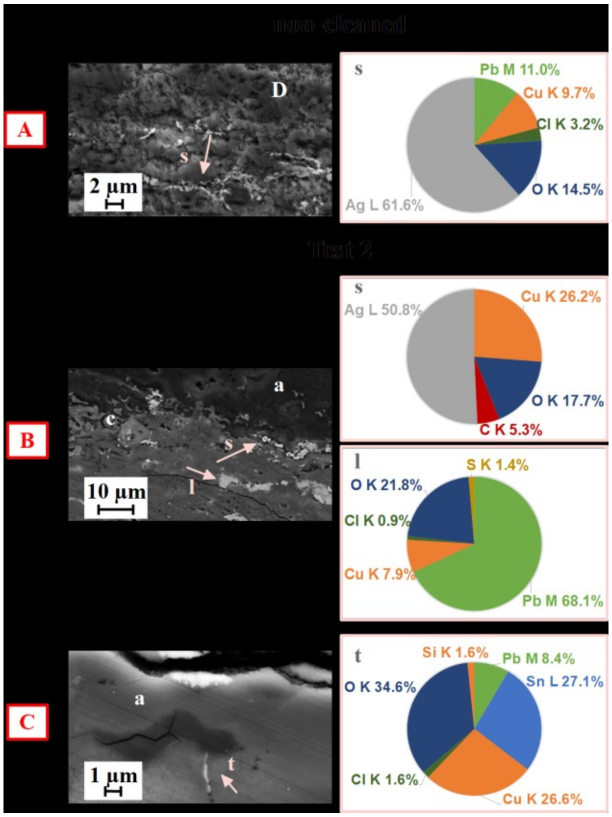

Fig. 13. Particulars (from Fig. 11) of the outer corrosion products layer of Coin 2, non-cleaned and laser-cleaned Test 2 cross-sections: FESEM-Supra-secondary electron images and respective punctual EDS analyses (pink arrows and letters highlight specific particulars points of analysis; amounts expressed in wt. %).

From these analyses, Coin 2 presented a thick multi-stratified corrosion product structure composed of three layers. The outer layer is composed of copper (II) compounds as hydroxycarbonates and hydroxychlorides (i.e. malachite and clinoatacamite) and other soil elements. The intermediate layer is mainly constituted by cuprous oxides, tin and lead compounds and, in the lower part, by a considerable amount of chlorine compounds. The inner corrosion products layer is mainly composed of stratified chlorine. So, Coin 2 is an original bronze coin buried in soil for a long time. Probably it was buried in an aggressive soil: it is an example of Type-2 corrosion structure [3,4] where the presence of cuprous chloride (CuCl) compounds, and in general high amount of Cl, favour a complete solubilisation of lead and tin from the alloy bringing to a progress of the Cl ions towards the bulk metal progressively destroying it, under particular environmental conditions [4,6]. This type of corrosion is called "bronze disease": the original alloy surface recedes, possibly until complete dissolution [11].

Also on this type of corrosion, the laser-cleaning procedure carried out at an irradiance of 1290.94 W/cm^2 was more efficient in the thickness reduction of the upper corroded layer, decreased the amount of soil elements, exposed an intermediate Cu(I) layer decreased in chlorine content and increased in the amount of copper. Indeed, the outer turquoise-green/green DF layer of Cu(II) compounds were almost totally ablated leaving the underlying intermediate layer of Cu(I) compounds. In the case of pits, the laser partially ablates the upper part of the outer corrosion layers without reach the bottom part of cradle-cavity.

3.5. Laser-cleaning effects considerations

In this study, the use of a scanning laser system was of extreme importance in order to perform laser-ablation treatments on a repeatable way on two different types of bronzes' corrosion products. The two archaeological bronze coins buried in soil for a long time were cleaned with the same laser conditions in order to investigate the laser effects on different real corrosion products. Indeed, systematic analyses showed that a coin presented more stable corrosion products, probably due to a burial soil less aggressive, that led the formation of complex stratified corrosion structure in two layers (Type-1 structure), while the other coin, probably buried in an aggressive soil for a long time, showed the presence of reactive corrosion products. Moreover, this last coin resulted affected by the so-called *bronze disease* and presented a stratified corrosion structure of the second type, characterised by a three-layer structure.

On both coins, the less intense laser condition (Test 1), optimised in previous works [27,31] for artificially corroded samples, revealed a low efficient ablation rate while three-times energy laser conditions (Test 2) resulted to be optimal on this kind of thick and dense stratified corrosion products.

The systematic chemical-physical study performed on the laser-cleaned cross-sections compared with the data of the non-cleaned ones, showed that Test 2 was able to completely remove the outer corrosion products layer encountered on the typical structure of both coins. In this case, cuprous oxide layer were present on the ablated surfaces. In the case of the ablation on cradle-cavities, on both coins, the laser was able to reduce the outer layer thickness but it was not able to reach the bottom of the pit and so the Cu(I) layers.

Since the laser is able to remove the unwanted products layer-by-layer, and thanks to the CAD-*like* software that enables complex surface treatments, more than one passes can be hypothesised for only this kind of areas.

The original corrosion products seem not to be altered in composition by the laser effects: the creation of new compounds during the ablation process was not detected.

To conclude, the laser-cleaning procedure, if properly performed and operating layer-by-layer, can be considered a safe and low-invasive cleaning procedure for archaeological Cu-Sn alloys, both presenting reactive and non-reactive corrosion products.

Advantages and disadvantages of the ablation procedure on reactive and non-reactive corrosion products should be carefully considered case by case with the restorers and the conservators, considering the final goal of each treatments on the specific artefacts. Each operation on a Cultural Heritage modify the established equilibrium of the artefacts with the environments: the effect of the exposure of reactive corroded layers to the air should be considered in conjunction with preservation procedures.

4. Conclusion

This study confirms the need of validating on real artefacts the scientific procedures performed on artificially-corroded samples. Moreover, a systematic and multi-technique compositional approach is useful in the determination of complex corrosion stratified structures were an unambiguous identification is not always possible: DF colour interpretation together with elementary, molecular and structural results are complementary techniques.

Laser-cleaning treatments were carried out on two archaeological bronze coins buried in soil for a long time, one characterised by stable corrosion products, presenting a Type-1 corrosion structure, and the other one characterised by reactive and dangerous corrosion products, presenting a Type-2 corrosion structure. Laser-cleaned and non-cleaned samples were both systematically characterised.

Being the archaeological corrosion layers thicker and denser than the artificially corroded ones, a three-times higher in fluence and irradiance values condition (Test 2) was more efficient in the removal of the unwanted corrosion layers on these real artefacts. Moreover, the laser-ablation does not seem to affect the composition of the ablated layers and, if the laser-parameters are correctly set, the ablation process leave a Cu(I) layer.

In addition to this, scanning laser systems are undoubtedly a powerful tool for performing rapid, precise and complex surface treatments in a repeatable way. In the case of cradle-cavities, thanks to this scanning system, it is possible to hypothesis to perform more than one laser passes (cycles) only on the interested area in order to reach an optimal ablation result.

In conclusion, by setting the right processing parameters, low-invasive and surface laser-cleaning procedures are possible on complex stratified corrosion layers, like those stable and dangerous encountered on archaeological Cu-Sn alloys buried in soil for centuries.

Acknowledgements

The authors would like to thank Dr. Jacopo Corsi for the donation of the bronze coins. Dr. Lahoz wishes to acknowledge professional support of the CSIC Interdisciplinary Thematic Platform ‘Open Heritage: Research and Society (PTI-PAIS)’. Acknowledges go also to Mauro Raimondo (Politecnico di Torino) for the FESEM-Merlin analyses.

Funding

This work was partially financial supported by the *European Federation of Corrosion* (EFC)

[EUROCORR Young Scientist Grant 2016].

References

[1] K.P. Fitzgerald, J. Nairn, A. Atrens, The chemistry of copper patination, Corros. Sci. (1998). https://doi.org/10.1016/S0010-938X(98)00093-6.

[2] D.C. Hemming, The production of artificial patination on copper, in: B. Floyd Brown, H.C. Burnett, W.T. Chase, M. Goodway, J. Kruger, M. Pourbaix (Eds.), Corros. Met. Artifacts. A Dialogue between Conserv. Archaeol. Corros. Sci., Washington: US Department of Commerce. National Bureau of Standards, 1977.

[3] L. Robbiola, C. Fiaud, Apport de l'analyse statistique des produits de corrosion à la compréhension des processus de dégradation des bronzes archéologiques, Rev. d'Archéométrie. (1992). https://doi.org/10.3406/arsci.1992.896.

[4] L. Robbiola, J.M. Blengino, C. Fiaud, Morphology and mechanisms of formation of natural patinas on archaeological Cu-Sn alloys, Corros. Sci. (1998). https://doi.org/10.1016/S0010-938X(98)00096-1.

[5] G.M. Ingo, T. De Caro, C. Riccucci, E. Angelini, S. Grassini, S. Balbi, P. Bernardini, D. Salvi, L. Bousselmi, A. Çilingiroğlu, M. Gener, V.K. Gouda, O.A.L. Jarrah, S. Khosroff, Z. Mahdjoub, Z.A.L. Saad, W. El-Saddik, P. Vassiliou, Large scale investigation of chemical composition, structure and corrosion mechanism of bronze archeological artefacts from Mediterranean basin, Appl. Phys. A Mater. Sci. Process. (2006). https://doi.org/10.1007/s00339-006-3550-z.

[6] C. Soffritti, E. Fabbri, M. Merlin, G.L. Garagnani, C. Monticelli, On the degradation factors of an archaeological bronze bowl belonging to a private collection, Appl. Surf. Sci. (2014). https://doi.org/10.1016/j.apsusc.2014.06.067.

[7] R. Hughes, Artificial patination, in: Met. Plat. Patination, 1993: pp. 1–18. https://doi.org/10.1016/b978-0-7506-1611-9.50005-4.

[8] T. Beldjoudi, F. Bardet, N. Lacoudre, S. Andrieu, A. Adriaens, I. Constantinides, P. Brunella, Surface modification processes on European Union bronze reference materials for analytical studies of cultural artefacts, Surf. Eng. 17 (2001) 231–235. https://doi.org/10.1179/026708401101517845.

[9] I. Constantinides, A. Adriaens, F. Adams, Surface characterization of artificial corrosion layers on copper alloy reference materials, Appl. Surf. Sci. 189 (2002) 90–101. https://doi.org/10.1016/S0169-4332(02)00005-3.

[10] F. Ospitali, C. Chiavari, C. Martini, E. Bernardi, F. Passarini, L. Robbiola, The characterization of Sn-based corrosion products in ancient bronzes: A Raman approach, in: J. Raman Spectrosc., 2012. https://doi.org/10.1002/jrs.4037.

[11] J. Muller, B. Laïk, I. Guillot, α-CuSn bronzes in sulphate medium: Influence of the tin content on corrosion processes, Corros. Sci. (2013). https://doi.org/10.1016/j.corsci.2013.07.025.

[12] E. Sidot, N. Souissi, L. Bousselmi, E. Triki, L. Robbiola, Study of the corrosion

behaviour of Cu-10Sn bronze in aerated Na2SO4 aqueous solution, Corros. Sci. (2006). https://doi.org/10.1016/j.corsci.2005.08.020.

[13] C. FOTAKIS, LASERS FOR ART’S SAKE!, Opt. Photonics News. (1995). https://doi.org/10.1364/opn.6.5.000030.

[14] R. Pini, S. Siano, R. Salimbeni, M. Pasquinucci, M. Miccio, Tests of laser cleaning on archeological metal artefacts, J. Cult. Herit. (2000). https://doi.org/10.1016/S1296-2074(00)00139-4.

[15] F. Landucci, R. Pini, S. Siano, R. Salimbeni, E. Pecchioni, Laser cleaning of fossil vertebrates: A preliminary report, J. Cult. Herit. (2000). https://doi.org/10.1016/S1296-2074(00)00141-2.

[16] S. Siano, J. Agresti, I. Cacciari, D. Ciofini, M. Mascalchi, I. Osticioli, A.A. Mencaglia, Laser cleaning in conservation of stone, metal, and painted artifacts: State of the art and new insights on the use of the Nd:YAG lasers, Appl. Phys. A Mater. Sci. Process. (2012). https://doi.org/10.1007/s00339-011-6690-8.

[17] C. Pelosi, L. Calienno, D. Fodaro, E. Borrelli, A.R. Rubino, L. Sforzini, A. Lo Monaco, An integrated approach to the conservation of a wooden sculpture representing Saint Joseph by the workshop of Ignaz Günther (1727-1775): Analysis, laser cleaning and 3D documentation, J. Cult. Herit. (2016). https://doi.org/10.1016/j.culher.2015.07.004.

[18] V. Tornari, V. Zafiropulos, A. Bonarou, N.A. Vainos, C. Fotakis, Modern technology in artwork conservation: A laser-based approach for process control and evaluation, Opt. Lasers Eng. (2000). https://doi.org/10.1016/S0143-8166(00)00068-3.

[19] J. Hildenhagen, K. Dickmann, Nd:YAG laser with wavelengths from IR to UV (ω, 2ω, 3ω, 4ω) and corresponding applications in conservation of various artworks, J. Cult. Herit. (2003). https://doi.org/10.1016/s1296-2074(02)01194-9.

[20] C. Fenic, R. Dabu, A. Stratan, C. Blanaru, C. Ungureanu, C. Luculescu, Preliminary studies of material surface cleaning with a multi-pulse passively Q-switched Nd:YAG laser, Opt. Laser Technol. (2004). https://doi.org/10.1016/S0030-3992(03)00144-0.

[21] L. Pereira-Pardo, C. Korenberg, The use of erbium lasers for the conservation of cultural heritage. A review, J. Cult. Herit. (2018). https://doi.org/10.1016/j.culher.2017.10.007.

[22] A. Dajnowski, Laser as a cleaning tool for the treatment of large-scale bronze monuments, in: Lasers Conserv. Artworks - Proc. Int. Conf. LACONA 7, 2008. https://doi.org/10.1201/9780203882085.ch48.

[23] A. Dajnowski, T. Ross, A.B. Craig, B. Dajnowski, New trends in art conservation, the use of lasers to clean as well as generate an augmented reality representation of an iconic public monument in bronze: The Alma Mater, Stud. Conserv. (2015). https://doi.org/10.1179/0039363015Z.000000000210.

[24] E. Drakaki, A.G. Karydas, B. Klinkenberg, M. Kokkoris, A.A. Serafetinides, E. Stavrou, R. Vlastou, C. Zarkadas, Laser cleaning on Roman coins, in: Appl. Phys. A Mater. Sci. Process., 2004. https://doi.org/10.1007/s00339-004-2657-3.

[25] M. Hrnjić, L. Angurel, R. Lahoz, S. Grassini, E. Angelini, N. Schiavon, G. de la Fuente, Near-IR laser cleaning of Cu-based artefacts: a comprehensive study of the methodology standardization, in: Proc. 1st Int. Conf. Metrol. Archaeol., 2015: pp. 389–394.

[26] B.A. Dajnowski, A. Sarzyński, A. Lins, T.P. Beebe Jr., J. Marczak, M. Strzelec, S. Ismat Shah, Z. Voras, J.L. Mass, R. Murray, Creating Laser Patinas on Copper Alloys : Origins of Colors and their Implications on Copper Alloys, in: Met. 2016 Proc. Interim Meet. ICOM-CC Met. Work. Gr. Sept. 26-30, 2016 New Delhi, India, 2017.

[27] E. Di Francia, R. Lahoz, D. Neff, E. Angelini, S. Grassini, Laser cleaning of Cu-based artefacts: Laser/corrosion products interaction, Acta IMEKO. 7 (2018). https://doi.org/10.21014/acta_imeko.v7i3.610.

[28] C. Fotakis, D. Anglos, V. Zafiropulos, S. Georgiou, V. Tornari, Lasers in the Preservation of Cultural Heritage: Principles and Applications, 2007.

[29] N. Antonopoulou-Athera, C. Kalathakis, E. Chatzitheodoridis, A.A. Serafetinides, Theoretical and experimental approach on laser cleaning of coins, SN Appl. Sci. (2019). https://doi.org/10.1007/s42452-019-0255-4.

[30] E. Di Francia, R. Lahoz, D. Neff, V. Rico, N. Nuns, E. Angelini, S. Grassini, Novel procedure for studying laser-surface material interactions during scanning laser ablation cleaning processes on Cu-based alloys, Appl. Surf. Sci. (2021). https://doi.org/10.1016/j.apsusc.2020.148820.

[31] E. Di Francia, L.A. Angurel, E. Angelini, S. Grassini, R. Lahoz, M. Parvis, Laser cleaning of archaeological bronze artefacts, in: Eur. Corros. Congr. EUROCORR 2016, 2016: pp. 1031–1039.

[32] D.A. Scott, Metallography and microstructure in ancient and historic metals. Getty Conservation Institute, Archetype , Marina del Rey, CA (US), 1991.

[33] F.J. Sarabia-Herrero, J. Martín-Gil, F.J. Martín-Gil, Metallography of ancient bronzes: Study of pre-roman metal technology in the Iberian Peninsula, Mater. Charact. (1996). https://doi.org/10.1016/s1044-5803(96)00067-8.

[34] R. Caron, R. Barth, D. Tyler, Metallography and Microstructures of Copper and Its Alloys, in: Metallogr. Microstruct. Vol. 9. ASM Int., 2004. https://doi.org/10.31399/asm.hb.v09.a0003772.

[35] Vander Voort, W. Baldwin, Metallography and Microstructures Handbook, ASM Int. (2004). https://doi.org/10.1361/asmhba0003771.

[36] P. Piccardo, B. Mille, L. Robbiola, Tin and copper oxides in corroded archaeological bronzes, in: Corros. Met. Herit. Artefacts Investig. Conserv. Predict. Long Term Behav., 2007. https://doi.org/10.1533/9781845693015.239.

[37] P. Piccardo, V. Bongiorno, S. Campodonico, Artistic patinas on ancient bronze statues, in: Corros. Conserv. Cult. Herit. Met. Artefacts, 2013. https://doi.org/10.1533/9781782421573.3.193.

[38] B. Lafuente, R.T. Downs, H. Yang, N. Stone, RRUFF^{TM} Project, Power Databases RRUFF Proj. Highlights Mineral. Crystallogr. T Armbruster R M Danisi, Eds. (2015).

[39] R.L. Frost, Raman spectroscopy of selected copper minerals of significance in corrosion, Spectrochim. Acta - Part A Mol. Biomol. Spectrosc. (2003). https://doi.org/10.1016/S1386-1425(02)00315-3.

[40] M. Bouchard-Abouchacra, Evaluation des Capacités de la Microscopie Raman dans la Caractérisation Minéralogique et Physico- chimique de Matériaux Archéologiques - Métaux, Vitraux & Pigments, École doctorale Sciences de la nature et de l'Homme - Évolution et écologie (Paris), 2001. https://www.theses.fr/2001MNHN0035.

[41] M. Bouchard, D.C. Smith, Catalogue of 45 reference Raman spectra of minerals concerning research in art history or archaeology, especially on corroded metals and coloured glass, in: Spectrochim. Acta - Part A Mol. Biomol. Spectrosc., 2003. https://doi.org/10.1016/S1386-1425(03)00069-6.

[42] G. Bertolotti, D. Bersani, P.P. Lottici, M. Alesiani, T. Malcherek, J. Schlüter, Micro-Raman study of copper hydroxychlorides and other corrosion products of bronze samples mimicking archaeological coins, Anal. Bioanal. Chem. (2012). https://doi.org/10.1007/s00216-011-5268-9.

[43] B. Lafuente, R. Downs, H. Yang, N. Stone, The power of databases: the RRUFF project. RRUFF ID: R050374.2 (cuprite), Highlights Mineral. Crystallogr. T Armbruster R M Danisi, Eds. Berlin, Ger. W. Gruyter,. (2015) 1–30. http://rruff.info/cuprite/display=default/R050374.

[44] B. Lafuente, R. Downs, H. Yang, N. Stone, The power of databases: the RRUFF project. RRUFF ID: R050638.3 (azurite), Highlights Mineral. Crystallogr. T Armbruster R M Danisi, Eds. Berlin, Ger. W. Gruyter. (2015) 1–30. https://rruff.info/azurite/display=default/R050638.

[45] R.L. Frost, W.N. Martens, L. Rintoul, E. Mahmutagic, J.T. Kloprogge, Raman spectroscopic study of azurite and malachite at 298 and 77 K, J. Raman Spectrosc. (2002). https://doi.org/10.1002/jrs.848.

[46] M. Ghoniem, The characterization of a corroded egyptian bronze statue and a study of the degradation phenomena, Int. J. Conserv. Sci. (2011).

[47] M. Quaranta, E. Catelli, S. Prati, G. Sciutto, R. Mazzeo, Chinese archaeological artefacts: Microstructure and corrosion behaviour of high-leaded bronzes, J. Cult. Herit. (2014). https://doi.org/10.1016/j.culher.2013.07.007.

[48] F. ENS Lyon, Handbook of Raman Spectra, (2020). http://www.ens-lyon.fr/LST/Raman/spectrum.php?nom=cotunnite.